Cancer Nanotechnology

RESEARCH Open Access

A novel pH- and glutathione-responsive drug delivery system based on in situ growth of MOF199 on mesoporous organic silica nanoparticles targeting the hepatocellular carcinoma niche

Jiaji Ling[1,2†], Yongmei Jiang[2†], Shaoying Yan[3†], Hao Dang[1], Huan Yue[1], Kanglin Liu[1], Linghan Kuang[2], Xingxin Liu[2] and Hua Tang[1*]

†Jiaji Ling, Yongmei Jiang and Shaoying Yan have contributed equally to this work

*Correspondence: tanghua86162003@cqmu.edu.cn

[1] Key Laboratory of Molecular Biology for Infectious Diseases (Ministry of Education), Department of Infectious Diseases, Institute for Viral Hepatitis, The Second Affiliated Hospital, Chongqing Medical University, 1 Yi Xue Yuan Road, Chongqing 400016, China
[2] Department of Laboratory Medicine, West China Second University Hospital, Sichuan University, Chengdu 610041, China
[3] Department of Clinical Laboratory, The First Affiliated Hospital of Nanchang University, Nanchang, Jiangxi, China

Abstract

Background: For people with advanced hepatocellular carcinoma (HCC), systemic chemotherapy remains the only choice of palliative treatment. However, chemotherapy efficacy is not effective due to its short blood circulation times, nonspecific cell and tissue biodistribution, and rapid metabolism or excretion from the body. Therefore, a targeted nanomedicine delivery system is urgently needed.

Methods: In order to improve the treatment efficiency of HCC, based on in situ growth of a copper metal organic framework on mesoporous organic silica nanoparticles, dual pH- and glutathione (GSH)-responsive multifunctional nanocomposites were synthesized as nanocarriers for enhanced HCC therapy. In this research, cellular uptake studies were performed using CLSM and Bio-TEM observations. Flow cytometry, AO-EB fluorescent staining, EdU test and Western blot were utilized to explore the apoptosis and proliferation process. In vivo imaging was employed to research the distribution of the nanocomposites in HCC tumor-bearing nude mice and the xenograft model of HCC tumor-bearing nude mice was applied to investigate the anti-tumor effects of drug-loaded nanocomposites in vivo.

Results: This newly constructed degradable nanocomposite DOX/SOR@SP94 and mPEG-anchored MONs@MOF199 (D/S@SPMM) has the benefits of controllable pore size, high encapsulation efficiency, and precise targeting. According to the results of in vivo imaging and anti-tumor studies, as well as pharmacokinetic research, D/S@SPMM possessed precise HCC tumor targeting and long-lasting accumulation properties at the tumor region. Compared with traditional chemotherapy and non-targeted drug delivery systems, anti-tumor efficiency was increased by approximately 10- and 5-fold, respectively. The nanocomposites exhibited excellent anti-tumor properties without inducing observable systemic toxicity, owing to efficient DOX and SOR loading and release as well as the HCC specific targeting peptide SP94.

Conclusions: The in vitro and in vivo anti-tumor results indicated that these nanocomposites could be an efficient nanomedicine for targeting HCC therapy.

Keywords: HCC therapy, Nanocarrier, pH-responsive, GSH-responsive, Multifunctional nanocomposites, Drug delivery

Introduction

Liver cancer is one of the most common malignant tumors in the world, especially in Asia, Africa, and southern Europe. Worldwide, the incidence rate of liver cancer is fifth in male malignant tumors, and second in mortality (Sayiner et al. 2019). Among women, the incidence rate of malignant liver tumors ranks ninth in all malignant tumors, and the mortality rate is sixth (Bertuccio et al. 2017). Hepatocellular carcinoma (HCC) is the main histological subtype of liver cancer, accounting for 90% of primary liver cancer (Kulik and El-Serag 2019). It is the third most common cause of cancer-related mortality in the world (Simon et al. 2020). Due to the lack of early-stage specific symptoms, most patients are not diagnosed with HCC until they reach an advanced stage (Samji et al. 2017). For these patients with advanced HCC, systemic chemotherapy remains the only choice of palliative treatment. However, chemotherapy efficacy is not expected due to its short blood circulation times, nonspecific cell and tissue biodistribution, and rapid metabolism or excretion from the body (Lyu et al. 2018).

In recent years, multifunctional nanoparticulate drug delivery systems (NDDSs) have made a great impact on overcoming the limitations of conventional chemotherapies (Cheng et al. 2012; Kim et al. 2018; Chatterjee et al. 2021; Mo et al. 2016; Laksee et al. 2020; Wang et al. 2017; Mirzaghavami et al. 2022), such as multifunctional theranostic nanoparticles based on exceedingly small magnetic iron oxide nanoparticles for T_1-weighted magnetic resonance imaging and chemotherapy (Shen et al. 2017), DNA origami as an in vivo drug delivery vehicle for cancer therapy (Zhang et al. 2014), multifunctional quantum dot DNA hydrogels (Zhang et al. 2017), and polyrotaxane-based supramolecular theranostics (Ji et al. 2019). In comparison with the traditional administration of free drugs, NDDSs have unique advantages including increased preferential tumor accumulation due to the enhanced permeability and retention (EPR) effect, which is characterized by microvascular hyperpermeability to circulating nanoparticles and impaired lymphatic drainage in tumor tissues (Lv et al. 2021; Golombek et al. 2018). However, the efficacy of this passive targeted delivery is low, and sufficiently high levels of drug concentrations at the tumor sites are not generally seen in practice. Therefore, active targeting is a more attractive approach (Ji et al. 2019; Golombek et al. 2018).

Mesoporous organic silica nanoparticles (MONs) are one of the most representative inorganic–organic hybrid mesoporous nanomaterials that has the potential to overcome the individual drawbacks of traditional organic and inorganic nanomaterials. For traditional organic nanomaterials, they are featured with high biocompatibility and biodegradability, but their stability is low and functionality is generally single. Comparatively, inorganic nanomaterials have high chemical/physiological stability and multifunctionality, but their biocompatibility and biodegradability are believed to be relatively low and still under debate. (Golombek et al. 2018; Ponton et al. 2020; Lei et al. 2019; Kong et al. 2021; Xu et al. 2022; Huang et al. 2017). MONs can be endowed with specific physicochemical properties and performances based on the intrinsic features of the integrated

organic fragments (Chen and Shi 2016; Yu et al. 2018). Therefore, MONs are envisioned to be one of the most promising nanomaterials over the next decade that can be utilized for many applications such as catalysis (Maity et al. 2019), adsorption (Teng et al. 2019), biosensing (Yang and Li 2020), molecular imaging and other biomedical applications (Croissant et al. 2018), especially drug/gene delivery. It has been well demonstrated that MONs can specifically respond to the reducing microenvironment intracellularly or within the tumor tissue due to the redox-responsive reaction caused by disulfide bonds (− S–S−) within these biological niches (Huang et al. 2017). Advanced metal organic framework nanoparticles (MOFs) are excellent carrier materials, which have the advantages of controllable pore size, low toxicity, high encapsulation efficiency, and mild synthesis conditions (Li et al. 2020, 2018; Wang et al. 2018; Cai et al. 2015). Research has shown that MOFs with redox-active metal ions, such as copper II (Cu^{2+}), favor effective reactions with GSH (glutathione). GSH concentrations in tumor tissues are higher than that in the blood circulation system and normal tissues, as is reported that tumor tissues exhibits at least fourfold GSH concentration compared with normal tissues (1–5 μmol/L), and the intracellular GSH concentration is then much higher and can reach up to 2–10 mmol/L (He et al. 2014). Upon reaction with GSH in cancer cells, dissociation of MOFs will occur, and the released drugs exert chemotherapy efficacy (Wang et al. 2019).

To enhance the targeting of HCC tissue and reduce the systemic toxicity of cheotmherapy drugs, we found that SP94 (SFSIIHTPILPL), a novel peptide identified by Lo et al. using a phage display technique, can specifically bind to various types of HCC cells, such as HepG2 and Huh7 (Lo et al. 2008). HCC cell membranes express an unknown target molecule that can be recognized by SP94 but not by hepatocytes (Jin et al. 2018). Ashley et al. conjugated SP94 with nanoparticle-supported lipid bilayers to improve therapeutic efficacy and reduce side effects, and it bound to HCC cells with high affinity due to the recruitment of SP94 targeting peptides. Their further results indicated that SP94 modified with MS2 virus-like particles exhibited a 10^4-fold higher affinity for HCC cells than for hepatocytes (Ashley et al. 2011).

Herein, we construct a drug delivery system with precise targeting to tumors utilizing dual-controlled multifunctional nanocomposites, DOX/SOR@SP94 and mPEG-anchored MONs@MOF199 (D/S@SPMM), based on in situ growth of copper MOF on MONs as nanocarriers for improved HCC therapy (Scheme 1). We hypothesize that multifunctional nanocomposites (D/S@SPMM) will provide superior anticancer effects on HCC cells due to their active targeting and drug release properties in comparison to non-targeted nanocomposites. As shown in the schematic diagram, MOF-199 is synthesized in situ on the surface of MONs. The HCC tissue-specific targeting peptide SP94 is then conjugated onto the MONs@MOF-199 via the formation of amide bonds. The poly (ethylene glycol) methyl ether (mPEG) is grafted onto the MONs@MOF-199 via an acid-labile β-thiopropionate linker. The anticancer drug doxorubicin hydrochloride (DOX) and sorafenib (SOR) are finally loaded onto the SP94 and mPEG-anchored MONs@MOF199 (SPMM), via hydrogen bonds, ionic bonds, and/or coordination bonds to construct the DOX and SOR-loaded SPMM (D/S@SPMM). When D/S@SPMM nanocomposites circulate in the bloodstream (pH 7.4), the hydrophilic polymer mPEG inhibits SP94 from coupling to healthy cells as the SP94 is hidden in the mPEG stealth layer.

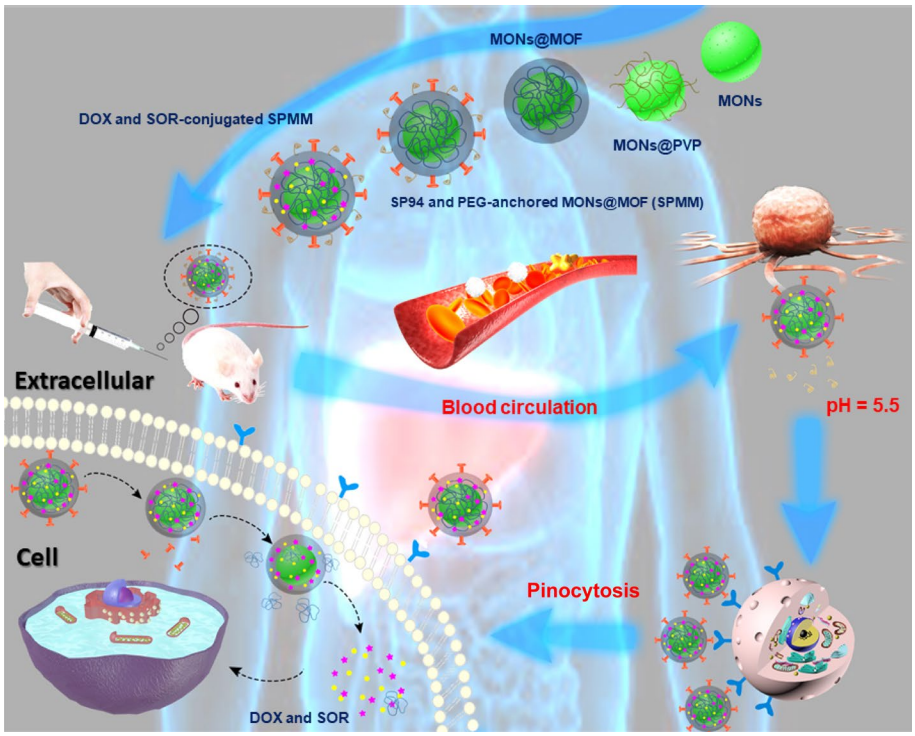

Scheme 1 Schematic illustration of the novel pH- and glutathione-responsive drug delivery system based on in situ growth of MOF199 on mesoporous organic silica nanoparticles targeting the hepatocellular carcinoma niche

However, in a mild acidic tumor microenvironment, the acid-labile β-thiopropionate linker degrades, which results in mPEG shedding from the nanocomposites (Shen et al. 2017; Zhang et al. 2015). Thus, the hidden SP94 is exposed and coupled to HCC cells. After being absorbed by HCC cells, the Cu^{2+} and disulfide bond (− S–S−) in MONs@MOF-199 nanoparticles react with GSH in a redox reaction, and the nanostructure collapses, releasing DOX and SOR to exude their anti-tumor effects. Finally, the endocytosed MONs are degraded into fragments, which can be excreted via active transport.

Materials and methods

Chemicals

Hexadecyl trimethyl ammonium bromide (CTAB), triethanolamine (TEA, ≥ 99%), tetraethyl orthosilicate (TEOS), anhydrous tetrahydrofuran (THF), and bis (triethoxysilyl propyl) disulfide (BTES) were purchased from Sigma-Aldrich. Doxorubicin hydrochloride (DOX), sorafenib (SOR) and glutathione (GSH) were bought from Solarbio. Polyvinylpyrrolidone (PVP) and (3-aminopropyl) triethoxysilane (APTES) were obtained from Hyclone. Benzene-1,3,5-tricarboxylate (BTC), glutaraldehyde (GA), anhydrous ethanol, phosphate buffer solution (PBS), sodium chloride (NaCl), and peptide SP94 (SFSIIHTPILPL) were purchased from Sangon Biotech (Shanghai, China). Poly(ethylene glycol) methyl ether (mPEG, M_w 5000), acryloyl chloride (AC, ≥ 97%), N,N-dimethylformamide (DMF), and cysteamine (CA) were purchased from Adamas-beta®, Shanghai Titan

technology co., LTD. All solvents were of gradient grade or high-performance liquid chromatography (HPLC) grade.

In vitro *cytotoxicity*

In vitro cytotoxicity of MONs@MOF-199, free DOX/SOR, D/S@MM, and D/S@SPMM were assayed with HepG2 cells. Cells were seeded in 96-well plates at a density of 5×10^3 cells per well and cultured in 5% CO_2 at 37 °C for 24 h. Then, the nanocapsules were added to the medium separately, and the cells were incubated in 5% CO_2 at 37 °C for 24 and 48 h. The DOX concentrations of the nanocapsules were 0.156, 0.312, 0.625, 1.2, 2.5, and 5 μM. At the end of incubation, 20 μL of MTS reagent was added to each well and incubated for another two hours, then analyzed with a microplate reader using a test wavelength of 490 nm within 10 min. The cytotoxicity is expressed as the percentage of cell viability compared to untreated control cells. The data are presented as the mean and standard deviation with six replicates.

Confocal imaging

First, 1×10^5 HepG2 cells were seeded onto glass cover slips in 12-well plates for 24 h. Subsequently, the medium was replaced by 1 mL of DMEM and incubated for 1 h. Then, DMEM was discarded and fresh cell culture containing PBS, MONs@MOF-199, free DOX/SOR, D/S@MM, and D/S@SPMM were added. Four hours later, cells were fixed by 4% formaldehyde for 15 min at room temperature. DAPI was then added to cells and incubated for 5 min in the dark. After cells were sealed with microscope glass slides, observations were performed using a confocal laser scanning microscope (CLSM).

Bio-TEM observations

The HepG2 cells were incubated with fresh cell culture and D/S@SPMM nanocomposites for 24 h. The cells were then washed three times with PBS and detached by incubation with 0.25% trypsin for 3 min. The cell suspension was centrifuged at 800 r/min for 5 min. After removal of the incubation medium, the HepG2 cells were collected in 1.5-mL centrifuge tubes and fixed by GA (1 mL, 2.5%) at 4 °C overnight. Follow-up work was completed by Beijing Zhongkebaice Technology Co., LTD.

Dual acridine orange/ethidium bromide (AO/EB) fluorescent staining

HepG2, Huh7, SK-Hep1, MHCC-97H, and 5637 cell lines were seeded in 12-well plates (1×10^5 cells/well) and incubated overnight, then cell culture medium was discarded and 2 mL of fresh cell culture medium containing PBS, MONs@MOF-199, free DOX/SOR, D/S@MM, and D/S@SPMM was added and incubated for 12 h. Before use, the AO and EB solutions were mixed up to get a working solution at a ratio of 1:1, and the working solution needed to be prepared immediately before use. The cell culture medium was removed, and the cells were washed twice with PBS to remove residual medium and non-adherent cells. The concentration of the working solution was 20 μL per milliliter of PBS, which was left at room temperature for 2–5 min before observing under a fluorescence microscope.

Acridine orange can penetrate cells with intact membranes, intercalation of DNA, and emit green fluorescence when combined with double-stranded DNA (Plemel et al. 2017).

However, ethidium bromide (EB) can only penetrate cells with damaged membranes, embed nuclear DNA, and emit orange fluorescence. Apoptotic cells develop enhanced staining, brighter fluorescence, and a uniform, round or condensed, mass-like structure. Non-apoptotic nuclei exhibit structure-like features with varying shades of fluorescence, and the two are easily distinguished. Under a fluorescent microscope, four types of cells could be seen: living cells (VN), with nuclear chromatin having a green and normal structure; early apoptotic cells (VA), with nuclear chromatin having a green shrinking or bead-like appearance; late apoptotic cells (NVA), where the nuclear chromatin is orange-red with a contraction or bead-like shape; and non-apoptotic dead cells (NVN), which had an orange-red nuclear chromatin with a normal structure. The dual acridine orange/ethidium bromide (AO/EB) staining method was repeated at least three times.

Cell proliferation study by the EdU test

1×10^5 HepG2 and SK-Hep1 cells were seeded onto glass cover slips in 12-well plates for 12 h. Subsequently, the medium was replaced with 1 mL of fresh cell culture containing PBS, MONs@MOF-199, free DOX/SOR, D/S@MM, and D/S@SPMM. After 12 h of incubation, a working concentration of EDU reagent was added and incubated for another 2.5 h. Then, cells were fixed for 15 min at room temperature by adding 4% formaldehyde. Next, 0.3% Triton X-100 was added to the cells and incubated for 10–15 min. Afterwards, 0.2 mL/well of click addictive solution was added to the cells and incubated for 30 min in the dark. After staining the nuclei with DAPI for 5 min, observations were performed using a confocal laser scanning microscope (CLSM) on cells that were sealed with a microscope glass slide.

Western blotting analysis

Ice-cold RIPA lysis buffer (Beyotime, Shanghai, China) including protease inhibitors was used to extract the total proteins from cells; quantification of proteins was carried out with the BCA reagent. Proteins were separated by SDS-PAGE on a 12% polyacrylamide gel and then electrophoretically transferred to a polyvinylidene fluoride membrane. Membranes were subsequently blocked with 5% non-fat milk in TBST buffer for 2 h at room temperature and incubated overnight at 4 °C with the appropriate primary antibodies as follows: anti-Bcl-2 antibody, anti-BAX antibody, anti-Cleaved Caspase 3 (Cl-Caspase 3) antibody, and anti-GAPDH antibody. Next, the membranes were incubated with correlated secondary antibodies (Proteintech, Wuhan, China) for 2 h at room temperature. Specific protein bands were detected using an ECL advanced western blotting detection kit and visualized by ChemiDoc XRS (Bio-Rad). Optical densities of bands in each blot were quantified using Image J Software and normalized with their respective control.

Pharmacokinetics in mice

BALB/c nude mice (4-week-old) were purchased from the Chinese Academy of Science, and all procedures for the in vivo nude mice study were approved by the Animal Care Committee of Chongqing Medical University. They were randomly divided into three groups (three mice per group) and injected intravenously through the tail vein with free DOX/SOR, D/S@MM, and D/S@SPMM, with 5 mg DOX/kg and 1 mg SOR/kg. At

predetermined time points (0.0833, 0.25, 0.5, 1, 2, 4, 8, 12, 24, and 48 h), about 0.2 mL of blood was collected from the tail vein in a heparinized tube after injection. Plasma was isolated by subsequent centrifugation at 3000 rpm for 10 min at 4 °C, then the supernatant was collected. The samples were detected using a microplate reader and UV–visible spectrophotometer for DOX and SOR determination. Pharmacokinetics parameters were calculated using DAS 2.0 software.

In vivo imaging study

To evaluate the tumor targeting ability of the nanodrugs, a mouse model bearing HepG2 cell-derived xenograft was established by subcutaneous injection of 5×10^6 HepG2 cells in the right flank of the mouse. When the tumor volume reached about 150 mm^3, mice were randomly divided into five groups (n = 5). Mice were injected with PBS, FITC, D/S@MM, and D/S@SPMM via the tail vein. In vivo imaging was performed on an in vivo imaging system at 1, 4, 8, 12, and 24 h post-injection.

In vivo anti-tumor efficiency

The xenograft liver tumor-bearing model was established on BALB/c nude mice by subcutaneous transplantation of 5×10^6 HepG2 cells/mouse in their right flank. When the volume of transplanted tumor reached approximately 150 mm^3, mice were randomly divided into five groups (five mice per group), injected with PBS, MONs@MOF-199, free DOX/SOR, D/S@MM, and D/S@SPMM (5 mg DOX/kg and 1 mg SOR/kg) via tail vein once every three days within an interval of 21 days. Thereafter, tumor growth was monitored, and tumor volume was calculated using the following equation:

$$V = (ab^2)/2,$$

where a and b indicate the width and length of the tumor, respectively.

Finally, after mice were killed, major organs including the heart, liver, spleen, lung, kidney and tumor were collected; and the volumes were measured and fixed with 4% paraformaldehyde for 7 days. Subsequently, these tissues were processed for routine H&E staining using standard methods. Ki-67 immunostaining was performed for tumor specimens in various groups according to the standard protocol.

Statistical analysis

Each experiment was carried out in triplicate. The experimental data analysis was conducted by using IBM SPSS Statistics software (Version 26.0) and Origin software (Version 8.5). All experimental data are represented as the mean ± standard deviation (SD). The level of statistical significance for all tests was set at $^{*}p < 0.05$, and $^{**}p < 0.01$.

Results and discussion

Synthesis and characterization

MONs, MOF-199, MONs@MOF-199, SPMM, and D/S@SPMM were fabricated according to the method described in supporting information. Transmission electron microscopy (TEM) was employed to characterize the morphology and the structure of the MONs (Fig. 1A–C), MOF-199 (Fig. 1D), MONs@MOF-199 (Fig. 1E), and SPMM (Fig. 1F). The particle size of SPMM was measured using dynamic light scattering (DLS)

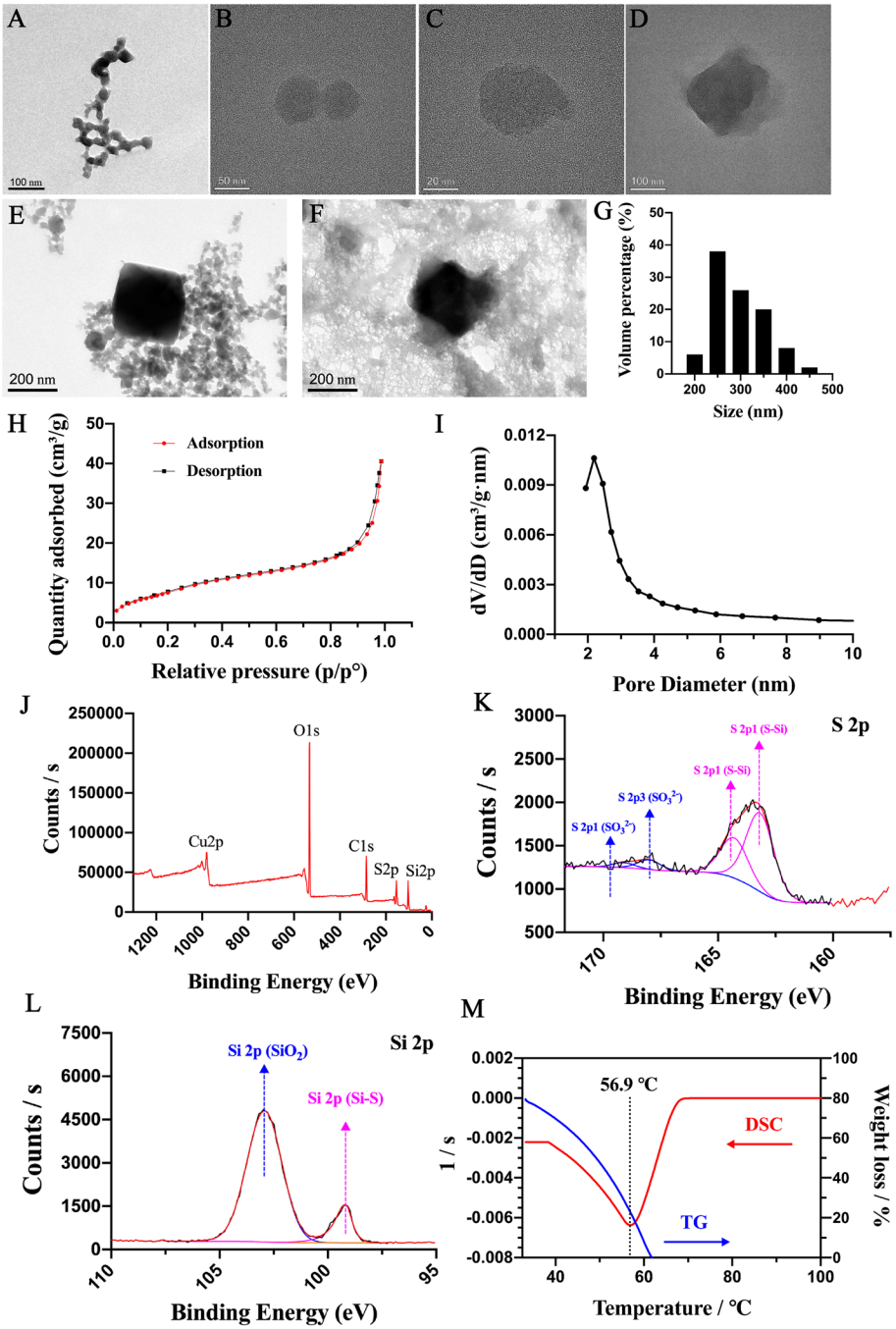

Fig. 1 Characterization of different nanocomposites. TEM images of MONs (**A-C**), MOF-199 (**D**), MONs@MOF-199 (**E**), and SPMM (**F**). **G** DLS experiments of SPMM. **H-I** N_2 adsorption–desorption isotherms of MONs. **J-L** XPS experiments of SPMM. **M** DSC-TG test of D/S@SPMM nanocomposites

experiments (Fig. 1G), and zeta potential of MONs@MOF-199, SPMM and D/S@SPMM were adopted to illustrate the preparation of this drug-loaded system, and results are presented in Additional file 1: Fig. S1. The results from TEM and DLS displayed that the particle size of MONs, MONs@MOF-199, and SPMM was about 50 nm, 200 nm, and 250 nm, respectively. As the outer structure of MONs, MOF-199 had the typical

characteristic of a MOF, porous structure. In our study, the pore size of MONs and successful incorporation of –S–S- were two key factors for loading and releasing nanodrugs. To confirm these two key points, N_2 adsorption–desorption isotherms and X-ray photoelectron spectroscopy (XPS) experiments were adopted. The results show that the pore diameter of MONs was about 2.5 nm (Fig. 1H–I) and –S–S– does exist in the nanocomposites (Fig. 1J–L). To explore the detailed thermal decomposition behaviors and kinetics of the nanocomposites, Differential scanning calorimetry–thermogravimetry (DSC–TG) was adopted (Zhou et al. 2020). The DSC–TG data displayed heat absorption and weight loss at around 56.9 °C (Fig. 1M) due to the organic component decomposition and the resultant CO_2 and SO_2 release, demonstrating its stability at body temperature.

We also performed a UV–vis spectrum analysis on a series of nanocomposite materials; the specific details are displayed in the supporting information (Additional file 1: Fig. S2). Collectively, the results support the successful synthesis of the D/S@SPMM nanocomposites.

Hemocompatibility and cytotoxicity

It is important to investigate the biocompatibility of the MONs, MONs@MOF-199, and SPMM nanocomposites with blood cells to guarantee the successful intravenous administration of drug-loaded nanocomposites. Hemolysis experiments of MONs, MONs@MOF-199, and SPMM were conducted according to previous methods. The hemolysis results showed that almost no hemolysis of RBCs could be detected in these three nanocomposites (Additional file 1: Fig. S5). We also performed hemolysis experiments on SPMM nanocomposites at different dilution ratios (Fig. 2A, B). It can be seen from the results that almost no hemolysis of RBCs could be detected in the samples of SPMM nanocomposites at different dilution ratios ranging from 10 to 1000. About 1.1% of hemolytic activities were distinguished at very high concentrations of 10 times dilution, much smaller than those of traditional nanoparticles (Singh et al. 2020). These data demonstrate that SPMM nanocomposites have excellent blood compatibility.

To evaluate the cytotoxicity of MONs@MOF-199, free DOX/SOR, D/S@MM, and D/S@SPMM, in vitro cytotoxicity tests were conducted with HepG2 cells by MTS assays. From Fig. 2C, D, we found that the difference of cell viabilities after 24 and 48 h of incubation was negligibly small. Apart from MONs@MOF-199, there was apparent cytotoxicity after incubation, especially for D/S@SPMM. The excellent biocompatibility (blood compatibility and low cytotoxicity) of the MONs@MOF-199 nanocomposites guarantees their practical applications for human beings as carriers in NDDSs. Besides, the cytotoxicity tests of the prepared nanocomposites towards hepatocellular carcinoma cell HepG2 and human normal liver cell L02 have been carried out to assess the targeting of D/S@SPMM, results are displayed in Additional file 1: Fig. S6.

Uptake of drug-loaded nanocomposites

The cellular internalization of five different NPs in HepG2 cells was monitored using CLSM after treatment for 4 h. As shown in Fig. 3A (c), although decreased cellular fluorescence was observed in the free DOX/SOR groups, the red fluorescence induced by DOX was distributed almost entirely in the cell nucleus, which could

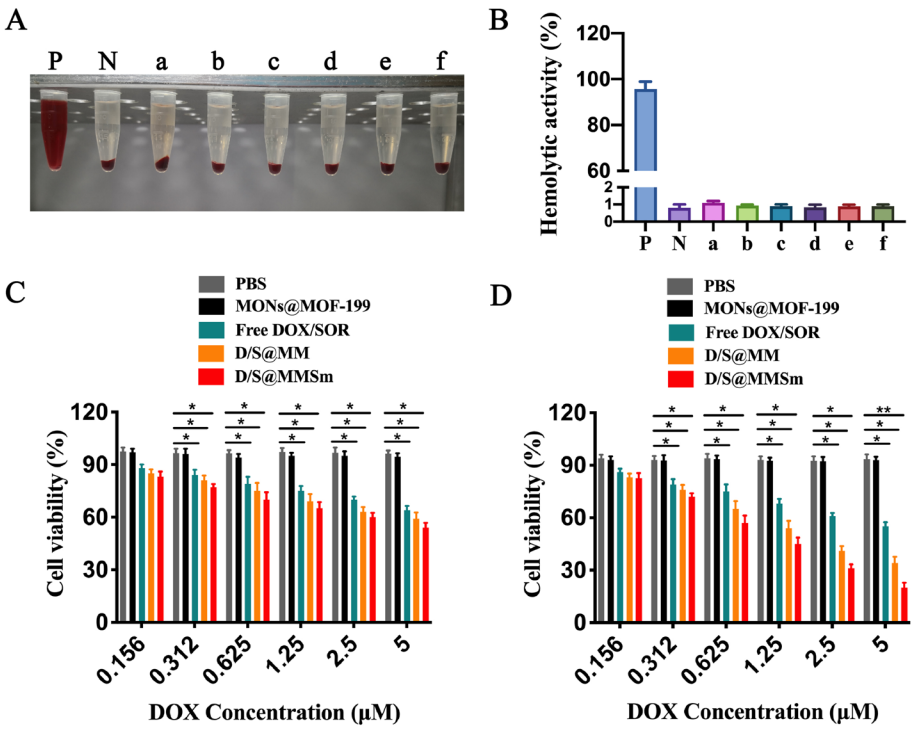

Fig. 2 Hemocompatibility and cytotoxicity of different nanocomposites. **A** The hemolysis assays of Ultrapure water (P), PBS (N), and SPMM nanocomposites at 10 (**a**), 50 (**b**), 100 (**c**), 250 (**d**), 500 (**e**), and 1000 (**f**) dilution ratios. **B** Visual histogram of the hemolysis tests. Cytotoxicity tests were conducted with HepG2 by MTS assays, with incubation for 24 h (**C**) and 48 h (**D**), $^{*}p < 0.05$, and $^{**}p < 0.01$

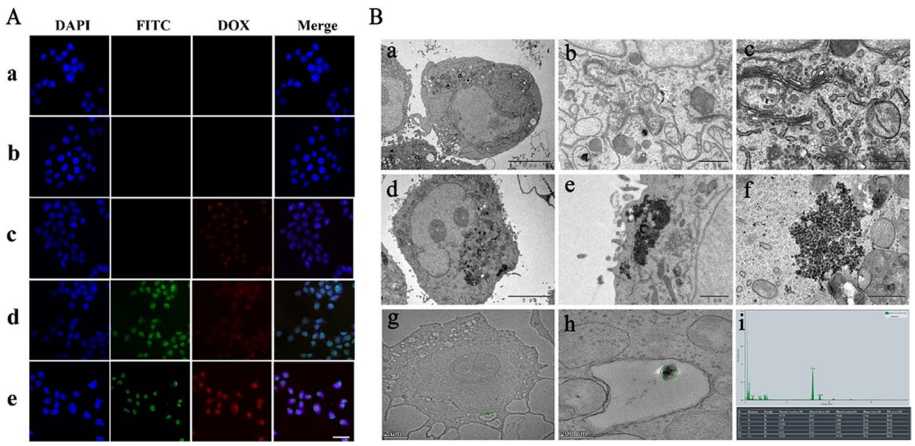

Fig. 3 Uptake of drug-loaded nanocomposites. **A** The cellular internalization of PBS (**a**), MONs@MOF-199 (**b**), free DOX/SOR (**c**), D/S@MM (**d**), and D/S@SPMM (**e**) were monitored using CLSM after treatment with HepG2 cells for 4 h; scale bar is 100 μm. **B** Bio-TEM of blank control group (**a-c**) and D/S@SPMM nanocomposites experimental group (**d-f**). EDS analysis of D/S@SPMM (**g-i**)

facilitate the rapid imbedding of DOX molecules in the DNA duplex. In accordance with the cytotoxicity results shown in Fig. 2C, D, increased fluorescence was observed in cells incubated with drug-loaded NPs compared to that of free drugs, especially D/S@SPMM (Fig. 3A (e)). This observation also demonstrated that the decoration of

the SP94 peptide on NPs could improve the binding of NPs with HepG2 cells and enhance the cellular uptake.

To explore the uptake process of the D/S@SPMM nanocomposites according to different incubation times, we established five groups: 0 h, 0.5 h, 2 h, 4 h, and 8 h. As displayed in Additional file 1: Fig. S7, FITC green fluorescence was observed at the first 0.5 h, and DOX red fluorescence was observed at 2 h, and the fluorescence intensity increased with the culture time. The DOX released from the D/S@SPMM can be divided into two stages. At stage one, the weakly bonded DOX will release from the nanocomposite quickly and accumulate in the cytoplasm region, then enter the nucleus gradually. At stage two, the strongly bonded DOX, together with the SPMM, transverse across the cytomembrane, then DOX enter the nucleus, combining with DNA. Hence, the red fluorescence of the cytoplasm was seen as early as 2 h after incubation. After 4 h of incubation, the red fluorescence focused and appeared in the nucleus. With the increase in incubation time, the fluorescence became stronger and more concentrated in the nucleus.

In addition, biological electron microscopy (Bio-TEM) was used to verify the uptake of nanocomposites by HepG2 cells and elemental mapping analysis using energy dispersive spectroscopy (EDS). We set fresh cell culture as the blank control group and D/S@SPMM nanocomposites as the experimental group. As illustrated in Fig. 3B (a-c), we did not observe any specific nanocomposites in HepG2 cells of the control group. In contrast, there was a distinct aggregation of nanoparticles in HepG2 cells of the experimental group (Fig. 3B, d–f). To distinguish glycogen particles in HepG2 cells, we selected two particle aggregation sites for EDS analysis, and the results showed that Cu, Si, S, C, N, and O elements were present in the nanoparticles, which indicated that the nanoparticles endocytosed by cells were D/S@SPMM nanocomposites (Fig. 3B, g–i).

In order to more visually observe degradation behavior and microstructure evolutions of D/S@SPMM in tumor cells, Bio-TEM was adopted, and the results are shown in Additional file 1: Fig. S9.

Apoptosis and proliferation processes

First, we implemented flow cytometry to compare the apoptosis induced by PBS, MONs@MOF-199, free DOX/SOR, D/S@MM, and D/S@SPMM. Annexin V-FITC and APC double staining was conducted to examine treated HepG2 cells. Flow cytometry-based quantification revealed the late apoptotic cell populations of PBS, MONs@MOF-199, free DOX/SOR, D/S@MM, and D/S@SPMM were $1.83 \pm 0.21\%$, $2.09 \pm 0.19\%$, $8.95 \pm 0.34\%$, $10.58 \pm 0.76\%$, and $11.54 \pm 0.87\%$, respectively (Additional file 1: Fig. S10). These results confirmed that D/S@SPMM had a higher therapeutic effect than free DOX/SOR and D/S@MM, $p < 0.05$. Consequently, D/S@SPMM could improve the therapeutic effect of DOX/SOR and might serve as a suitable NDDS.

Fluorescence images of HepG2, Huh7, SK-Hep1, MHCC-97H, and 5637 cell lines treated by five different groups are shown in Fig. 4A. It is known that AO can enter living cells with intact cell membranes and embed into DNA, making the cell nuclei be visualized by a bright green color. EB is unable to enter the live cells, but it can enter the dead cell membrane and the nuclei. Therefore, the dead and late apoptosis cells are stained a bright red color. In this work, untreated cells, PBS, and MONs@

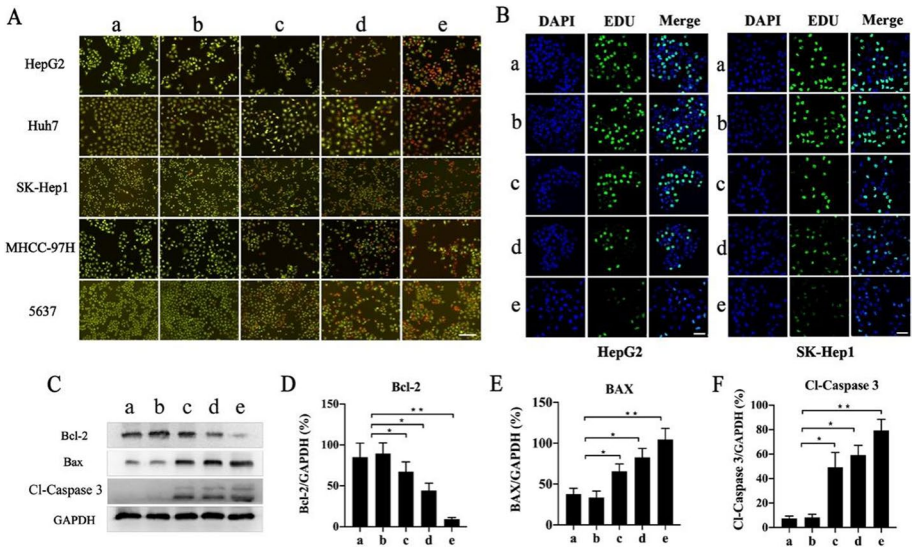

Fig. 4 Apoptosis and proliferation process. **A** AO-EB fluorescent staining assay; scale bar is 200 μm. **B** Cell proliferation study by EdU test; scale bar is 200 μm. **C-F** Western blot analysis of Bcl-2, BAX, and Cl-Caspase 3 expression, * represents $p < 0.05$ and ** represents $p < 0.01$. PBS (**a**), MONs@MOF-199 (**b**), free DOX/SOR (**c**), D/S@MM (**d**), and D/S@SPMM (**e**)

MOF-199-treated cells were bright yellow-green, suggesting nearly no apoptosis of cells treated by the two treatments. However, the cells treated with free DOX/SOR, D/S@MM, and D/S@SPMM (10 μg mL^{-1}) exhibited a gradual increase in red fluorescence signal, suggesting predominant apoptosis after 12 h of incubation. The red color of the cells treated with the D/S@SPMM group was more profound than that of free DOX/SOR and D/S@MM ($p < 0.05$), suggesting that D/S@SPMM had the maximum toxicity for HCC cell lines. This phenomenon was not tenable in non-HCC cell lines, such as 5637 cells, because of the HCC-specific targeting peptide SP94 existing in nanocomposites.

After studying the effects of apoptosis, we further verified whether HCC cell proliferation could be inhibited by the DOX/SOR encapsulated in the biological macromolecules. An EdU cell proliferation assay was performed with HepG2 and SK-Hep1 cells. As illustrated in Fig. 4B and Additional file 1: Fig. S11, cell proliferation was inhibited by incubation with the D/S@SPMM nanocomposites. Notably, D/S@SPMM showed a higher inhibitory effect on proliferation than the other four groups in both cells ($p < 0.05$). Thus, we speculated that due to the sustained release property, both D/S@MM and D/S@SPMM nanocomposites displayed higher anti-proliferation effects than the free DOX/SOR.

Furthermore, to confirm whether the apoptosis- and proliferation-related proteins, such as Bcl-2, BAX, and Cl-Caspase 3, were affected after five different treatments, western blotting analysis was performed. As shown in Fig. 4C, compared with the control groups, free DOX/SOR and NPs groups, the D/S@MM group expressed considerably less proliferation-related protein Bcl-2 and more apoptosis-related proteins, namely, BAX and Cl-Caspase 3. In particular, the D/S@SPMM group had the most obvious change in Bcl-2, BAX and Cl-Caspase 3 proteins when compared with the other four groups. Using GAPDH as an internal reference, the related protein expression levels are

displayed in Fig. 4D–F. Collectively, these results indicate that D/S@SPMM nanocomposites inhibit the proliferation of liver cancer cells and promote apoptosis.

Pharmacokinetics study in vivo

The blood pharmacokinetics of free DOX/SOR, D/S@MM, and D/S@SPMM were monitored in tumor-free BALB/c nude mice. The blood samples were collected at 0.0833, 0.25, 0.5, 1, 2, 4, 8, 12, 24, and 48 h after injection of the above three nanocomposites via tail vein followed by determination of the plasma concentrations of DOX and SOR. As illustrated in Fig. 5A, B, the elimination of DOX and SOR in free drugs was quick, as only low concentrations of the drugs could be detected at 12 h. On the contrary, drugs loaded in MONs@MOF-199 and SPMM exhibited prolonged retention—we could detect trace drugs until 36 h in the D/S@SPMM group. Among our detection time points, there was no statistical difference in the first four hours after intravenous injection, there were statistical differences at 4 h, 8 h, 12 h and 16 h, but no statistical difference was shown after 16 h. These results suggest that the encapsulation of drugs in SPMM nanocomposites give rise to longer retention in blood circulation and therefore better bioavailability.

In vivo *distribution of the nanocomposites*

To investigate the in vivo distribution of the D/S@SPMM nanocomposites, FITC was grafted into the nanocomposites. In addition, we set PBS, FITC, and D/S@MM as the controls. These four different treatments were intravenously injected into a xenograft model of HCC tumor-bearing nude mice via tail veins, and fluorescence distribution in vivo was captured at 1, 4, 8, 12, and 24 h post-injection. As shown in Fig. 6, a strong fluorescence signal from the entire mouse body was observed in FITC- (Fig. 6B), D/S@MM- (Fig. 6C), and D/S@SPMM- (Fig. 6D) treated groups 1 h after the injection, which may be attributed to the blood circulation. Along with prolonged circulation time, the fluorescence intensity in the tumor site of the D/S@SPMM-treated group gradually increased after 8 h post-injection, indicating that it can gradually accumulate at the tumor site. The fluorescence signal in the mice that received free FITC and D/S@MM quickly decayed after the early time points, which may be due to efficient renal clearance, such that there was no accumulation in tumors. As a control group, the PBS group did not show any fluorescence during the entire monitoring process (Fig. 6A). At 24 h

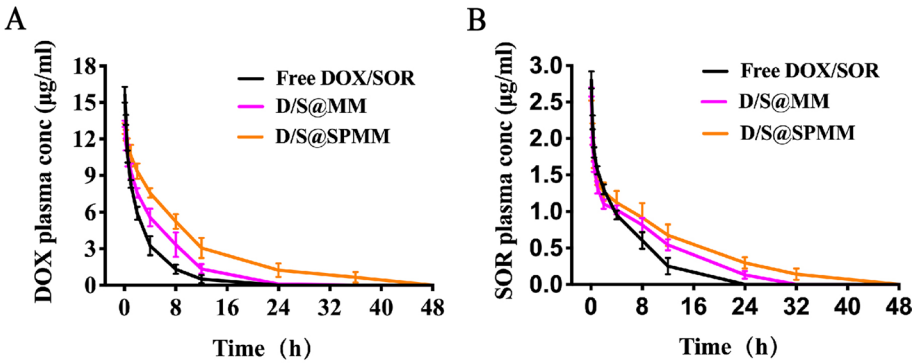

Fig. 5 Blood pharmacokinetics of DOX (**A**) and SOR (**B**) were monitored in tumor-free BALB/c nude mice after intravenously injected with free DOX/SOR, D/S@MM, and D/S@SPMM

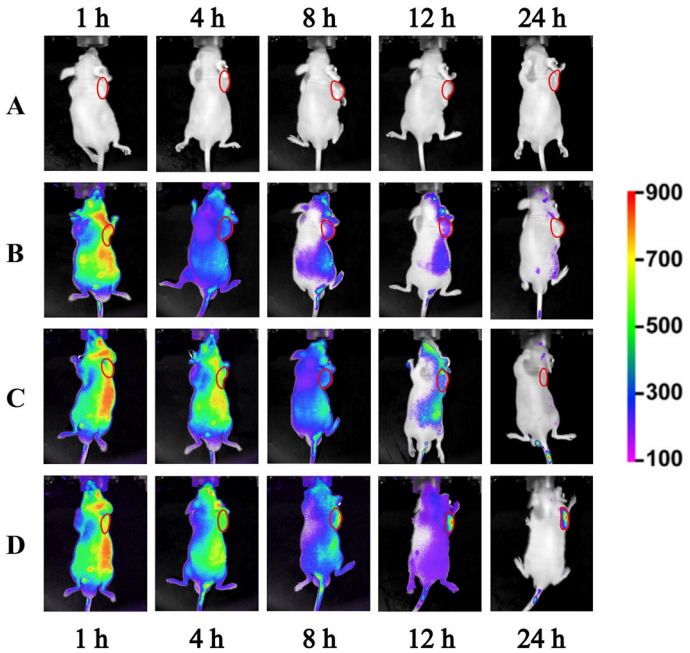

Fig. 6 In vivo distribution of the nanocomposites. Mice were injected with PBS (**A**), FITC (**B**), D/S@MM (**C**), and D/S@SPMM (**D**) via tail vein. In vivo imaging was performed on an in vivo imaging system at 1, 4, 8, 12, and 24 h post-injection

post-injection, the tumor in the D/S@SPMM-treated group maintained a strong fluorescence signal, suggesting good targeting and retention ability of the D/S@SPMM nanocomposites in the tumor.

In vivo *anti-tumor effects of drug-loaded nanocomposites*

Inspired by the excellent in vitro therapeutic effects of D/S@SPMM, we evaluated the anticancer potentials of these nanocomposites in vivo. As shown in Fig. 7A. PBS, MONs@MOF-199, free DOX/SOR, D/S@MM, and D/S@SPMM were injected into the HCC tumor-bearing mice (~150 mm^3) via tail vein every two days. To record the physical condition of these nude mice, tumor volume and mice weight were accurately measured every two days and are displayed in Fig. 7B, C.

All mice were killed when the tumor volume of the mice injected with PBS reached about 1500 mm^3. As shown in Fig. 7D, a significant inhibition of tumor growth was observed in the injected mice, with D/S@SPMM leading to the most efficient anti-tumor effect and improved survival rate (Fig. 7E). In addition, free DOX/SOR and D/S@MM also showed some suppression of tumor growth, but not as distinct as that in the D/S@SPMM therapy group. Notably, the control groups, PBS and MONs@MOF-199 not only had no effect on tumor treatment, but also did not improve the survival rate. Such excellent therapeutic effect could be attributed to the pH and GSH dual stimulus responsive D/S@SPMM nanocomposites, as well as the therapeutic pathways of each compound that somehow improve cell death. These results illustrate that D/S@SPMM nanocomposites could achieve efficient anti-tumor therapy and improve survival rate at the same time.

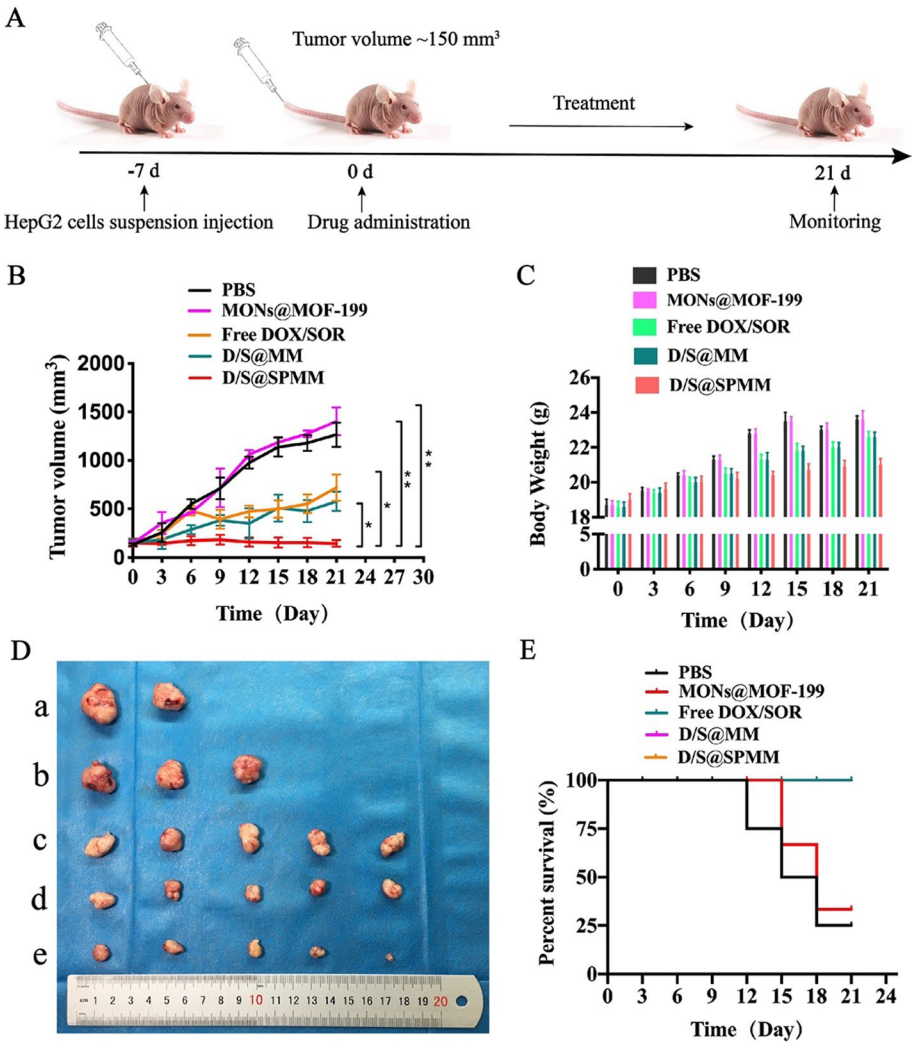

Fig. 7 In vivo anti-tumor effects of drug-loaded nanocomposites. **A** Schematic illustration of this in vivo anti-tumor efficiency experiment. Tumor volume (**B**) and mice weight (**C**) were accurately measured every two days, * represents $p < 0.05$ and ** represents $p < 0.01$. **D** All mice were humanely killed when the tumor volume of the mice injected with PBS reached about 1500 mm^3, PBS (**a**), MONs@MOF-199 (**b**), free DOX/SOR (**c**), D/S@MM (**d**), and D/S@SPMM (**e**). **E** survival rate

Effect of D/S@SPMM on systemic toxicity and proliferation in tumor tissues

To investigate the systemic toxicity of D/S@SPMM, murine blood and major organs including the heart, liver, spleen, lung, kidney, and tumor were collected after mice were humanely killed. Blood biochemical tests can monitor the response to exogenous toxic exposure and are widely used in disease diagnoses of the liver and kidney. The changes in biochemical parameters of the PBS, MONs@MOF-199, free DOX/SOR, D/S@MM, and D/S@SPMM groups are presented in Table 1. Compared with the control group, the test groups showed that no severe hepatotoxicity occurred ($p > 0.05$), illustrating that its damage to the liver was negligible, especially the D/S@SPMM group.

Subsequently, Hematoxylin and eosin (H&E) staining was performed to evaluate the systemic toxicity and anti-tumor efficiency. As shown in Fig. 8, no noticeable

Table 1 Effect of control groups, free DOX/SOR and NPs groups on serum levels of total protein, alanine aminotransferase, aspartate aminotransferase, alkaline phosphatase and lactate dehydrogenase

Group	TP (g/L)	ALT (U/L)	AST (U/L)	AKP(U/L)	LDH (U/L)
PBS	65.33 ± 5.73	33.33 ± 4.19	39.33 ± 4.11	75.33 ± 7.85	174.67 ± 12.28
MONs@MOF-199	64.33 ± 4.50	35.67 ± 3.68	39.00 ± 4.90	80.00 ± 10.03	189.33 ± 7.13
free DOX/SOR	59.67 ± 6.24	29.33 ± 4.50	30.67 ± 3.86	89.00 ± 9.09	234.67 ± 11.09
D/S@MM	61.33 ± 7.59	27.00 ± 2.16	32.67 ± 5.31	83.33 ± 4.19	197.67 ± 16.36
D/S@SPMM	64.33 ± 6.13	32.33 ± 4.19	37.00 ± 4.55	76.33 ± 4.92	181.67 ± 14.06

TP total protein; *ALT* alanine aminotransferase; *AST* aspartate aminotransferase; *AKP* alkaline phosphatase; and *LDH* lactate dehydrogenase

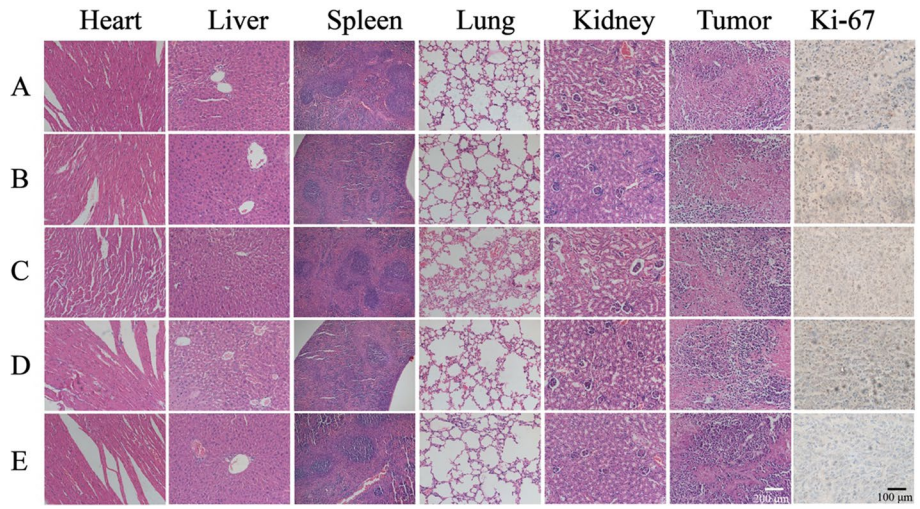

Fig. 8 Effect of D/S@SPMM on systemic toxicity and proliferation in tumor tissues. PBS (**A**), MONs@MOF-199 (**B**), free DOX/SOR (**C**), D/S@MM (**D**), and D/S@SPMM (**E**)

morphological changes of the above organs were observed among these five groups. Severe tumor cellular damage was observed in the group treated with D/S@SPMM (Fig. 8E), while the other four groups only showed limited cellular destruction (Fig. 8A–D). By contrast, tumor cells in the control group (PBS) retained their normal morphology (Fig. 8A). These results confirm that the D/S@SPMM nanocomposites not only exhibit no noticeable systemic toxicity but are also highly efficient for tumor therapy.

Finally, to further detect the proliferation efficiency of D/S@SPMM nanocomposites in tumor tissues, Ki-67 immunostaining was performed. As shown in Fig. 8**,** these five treatments exhibited **s**ignificant differences. In the PBS group, tumor cell proliferation efficiency was the highest (Fig. 8A) and lowest in the D/S@SPMM group (Fig. 8E). This phenomenon could be attributed to the effect of DOX and SOR encapsulated in the multifunctional nanocomposites. The Ki-67 immunostaining result was in accordance with the findings of in vivo inhibition of tumor growth (Fig. 7). These results fully support the D/S@SPMM nanocomposites as having excellent anti-tumor properties without systemic toxicity.

Discussion

In this study, based on in situ growth of a copper metal organic framework on mesoporous organic silica nanoparticles, dual pH- and GSH-responsive multifunctional nanocomposites were established as nanocarriers to load DOX and SOR for HCC therapy. We hypothesize that multifunctional nanocomposites (D/S@SPMM) will provide superior anticancer effects on HCC cells due to their active targeting and drug release properties in comparison to non-targeted nanocomposites. And through extensive experiments, we showed that the newly synthesized degradable nanocomposite, D/S@SPMM, possessed precise HCC tumor targeting and long-lasting accumulation properties at the tumor region. The nanocomposites possessed excellent anti-tumor properties without inducing observable systemic toxicity in vivo due to excellent blood compatibility and efficient drug loading and release, in addition to the HCC specific targeting peptide SP94.

As shown in the schematic diagram, MOF-199 is synthesized in situ on the surface of MONs. The HCC tissue-specific targeting peptide SP94 is then conjugated onto the MONs@MOF-199 via the formation of amide bonds. The poly (ethylene glycol) methyl ether (mPEG) is grafted onto the MONs@MOF-199 via an acid-labile β-thiopropionate linker. The anticancer drug doxorubicin hydrochloride (DOX) and sorafenib (SOR) are finally loaded onto the SP94 and mPEG-anchored MONs@MOF199 (SPMM), via hydrogen bonds, ionic bonds, and/or coordination bonds to construct the DOX and SOR-loaded SPMM (D/S@SPMM). When D/S@SPMM nanocomposites circulate in the bloodstream (pH 7.4), the hydrophilic polymer mPEG inhibits SP94 from coupling to healthy cells as the SP94 is hidden in the mPEG stealth layer. However, in a mild acidic tumor microenvironment, the acid-labile β-thiopropionate linker degrades, which results in mPEG shedding from the nanocomposites (Lo et al. 2008; Shen et al. 2017). Thus, the hidden SP94 is exposed and coupled to HCC cells. After being absorbed by HCC cells, the Cu^{2+} and disulfide bond (–S–S–) in MONs@MOF-199 nanoparticles react with GSH in a redox reaction, and the nanostructure collapses, releasing DOX and SOR to exude their anti-tumor effects. Finally, the endocytosed MONs is degraded into fragments, which can be excreted via active transport.

This innovatively constructed drug delivery system with precise targeting to HCC tumors, and it shows excellent anti-tumor effects both in vivo and in vitro. As depicted in our schematic diagram, MOF-199 is synthesized in situ on the surface of MONs. The HCC tissue-specific targeting peptide SP94 is then conjugated onto the MONs@MOF-199 via the formation of amide bonds. Then mPEG is grafted onto the MONs@MOF-199 via an acid-labile β-thiopropionate linker. The anticancer drug DOX and SOR are finally loaded onto SPMM via hydrogen bonds, ionic bonds, and/or coordination bonds to construct D/S@SPMM. When D/S@SPMM nanocomposites circulate in the bloodstream (pH 7.4), the hydrophilic polymer mPEG inhibits SP94 from coupling to healthy cells as the SP94 is hidden in the mPEG stealth layer. However, in a mild acidic tumor microenvironment, the acid-labile β-thiopropionate linker degrades, which results in mPEG shedding from the nanocomposites. Thus, the hidden SP94 is exposed and coupled to HCC cells. After being absorbed by HCC cells, the Cu^{2+} and disulfide bond (-S–S-) in MONs@MOF-199 nanoparticles react with GSH in a redox reaction, and the nanostructure collapses, releasing DOX and SOR to exude their anti-tumor effects.

Finally, the endocytosed MONs is degraded into fragments, which can be excreted via active transport.

With the rapid development of nanomedicine in recent years, there are many NDDSs systems that have been widely used in anti-tumor therapy. For instance, Kamel et al. proposed the design of inhalable dry powder nanocomposites of dual-targeted hybrid lipid–zein NPs for co-delivery of genistein and all-trans retinoic acid to lung cancer cells (Kamel et al. 2020). Sardoiwala's study demonstrates that hypericin-loaded transferrin nano-formulations (HTfNPs) enhance the photodynamic therapeutic efficiency against CRC by inducing PP2A-mediated BMI1 ubiquitination/degradation (Sardoiwala et al. 2020). Sharafaldin et al. developed a multifunctional nanoparticle composed of biocompatible factors (SPION, Au, CS, and FA) and analyzed its ability to reduce DOX toxicity as well as its applicability for targeted cancer cell therapy (Al-Musawi et al. 2020). Yang et al. constructed an MOF structure on the surface of MoS_2 to prepare a versatile theranostic agent for targeted cancer therapy (Yang et al. 2021). In Xie's research, layer-by-layer (LbL) self-assembly technology was used for the preparation of chitosan/carboxymethylcellulose functionalized $mMoS_2$ nanocomposites to promote the development of tumor therapy (Xie et al. 2021). However, due to their systemic toxicity, low drug loading efficiency, and nonspecific targeting for tumor cells, anti-tumor efficacy is not ideal.

An increasing number of nanocomposites have been used in drug delivery systems to treat tumors over the past decade, and promising results have been achieved (Xie et al. 2021). The novel NDDSs proposed in this study are a powerful method for the treatment of HCC in vivo and in vitro, as they demonstrated higher targeting capability and more effective than clinical chemotherapy. And encapsulation of drugs in SPMM nanocomposites could not only longer drugs retention time in blood circulation, but also accurately target tumor tissues and reduce systemic toxicity.

Although sufficient experiments have been carried out in the present work, including experiments that confirm the favorable properties of the D/S@SPMM material and its tumor treatment efficiency in vivo and in vitro, there are still shortcomings. For example, in exploring the role of D/S@SPMM in proliferation and apoptosis, we only analyzed proliferation and apoptosis-related proteins (Bcl-2, BAX, and Cl-Caspase 3) without studying the molecular mechanisms. Similarly, in the in vivo anti-tumor effects of drug-loaded nanocomposites section, due to limited conditions, we recorded the weight and volume of the tumor, and quantitative research on molecular and protein levels were neglected. As such, although the present research experimental results can well support the idea of this paper, it can be further improved. For example, in the future, the synthesis process of promising vehicles for D/S@SPMM should be optimized, so that its surface composition and particle size can be tuned to exploit the enhanced permeability and retention effect, as well as promote the circulation of D/S@SPMM nanocomposites in blood.

Collectively, the in vitro and in vivo anti-tumor results indicated that these nanocomposites could be an efficient nanodrug for targeting HCC therapy. The in vitro and in vivo anti-tumor results also revealed that D/S@SPMM nanocomposites may be effective and attractive in vivo application prospects. Moreover, we believe that more efficient nanomedicine vehicles will be designed in other more diverse, safe, and

efficient ways for clinical anti-tumor treatment. The nanocomposite itself may be the most suitable drug, through specific pH, GSH, ROS, or other responses to the tumor microenvironment, acting as a nanomedicine and activating anti-tumor related pathways to exert anti-tumor effects.

Conclusions

In conclusion, we successfully constructed a dual pH- and GSH-responsive multifunctional nanocomposite D/S@SPMM, based on in situ growth of copper MOFs on porous organic silica nanoparticles, as nanocarriers for improved HCC therapy. This newly synthesized, degradable nanocomposite possessed precise HCC tumor targeting and long-lasting accumulation properties at the tumor region. Particularly, it had excellent anti-tumor properties without inducing observable systemic toxicity owing to efficient DOX and SOR loading and release as well as the HCC specific targeting peptide SP94. The in vitro and in vivo anti-tumor results indicated that it could serve as an efficient nanodrug for target HCC therapy. The biochemical and histopathological tests also revealed that these nanocomposites might be effective and have attractive in vivo application prospects. We sincerely hope that through specific modification, these proposed NDDSs can be used for the efficient treatment of various cancers.

Supplementary Information

The online version contains supplementary material available at https://doi.org/10.1186/s12645-022-00139-6.

Additional file 1. Combined effects, drug loading, releasing and degradation behaviors.

Acknowledgements
Not applicable.

Author contributions
Conceptualization—HT, data curation—JL, formal analysis—YJ, SY, funding acquisition—HT, SY, XL, investigation—JL, methodology—YJ, HD, HY, KL, project administration—HT, resources—YJ, software—HY, KL, LK, supervision—HT, validation—HD, HY, KL, visualization—JL, HT, writing—original draft—JL, writing—review and editing—HT. All authors read and approved the final manuscript.

Funding
This study was supported by the Key Laboratory of Infectious Diseases, CQMU (202004), the Grant from Science and Technology Bureau of Chengdu (No. 2021-YF05-01691-SN), the Province Natural Science Foundation of Sichuan Province (2022NSFSC1420), and the West China Second University Hospital Clinical Research Fund (No.KL105).

Availability of data and materials
The datasets used or analyzed during the current study are available from the corresponding author on reasonable request.

Declarations

Ethics approval and consent to participate
This study was performed in accordance with the regulations of Chongqing Medical University Standing Committee on human biomedical research and animal experiments, and were approved by the Institutional Committee.

Consent for publication
All authors have agreed to publish this manuscript.

Competing interests
The authors declare that they have no competing interests. No financial conflict of interest was reported by the authors of this paper.

Received: 30 June 2022 Accepted: 30 September 2022
Published online: 16 October 2022

References

Al-Musawi S, Albukhaty S, Al-Karagoly H, Almalki F (2020) Design and synthesis of multi-functional superparamagnetic core-gold shell coated with chitosan and folate nanoparticles for targeted antitumor therapy. Nanomaterials. https://doi.org/10.3390/nano11010032

Ashley CE, Carnes EC, Phillips GK, Durfee PN, Buley MD, Lino CA, Padilla DP, Phillips B, Carter MB, Willman CL, Brinker CJ, Caldeira Jdo C, Chackerian B, Wharton W, Peabody DS (2011) Cell-specific delivery of diverse cargos by bacteriophage MS2 virus-like particles. ACS Nano 5(7):5729–5745. https://doi.org/10.1021/nn201397z

Bertuccio P, Turati F, Carioli G, Rodriguez T, La Vecchia C, Malvezzi M, Negri E (2017) Global trends and predictions in hepatocellular carcinoma mortality. J Hepatol 67(2):302–309. https://doi.org/10.1016/j.jhep.2017.03.011

Cai W, Chu CC, Liu G, Wang YX (2015) Metal-organic framework-based nanomedicine platforms for drug delivery and molecular imaging. Small 11(37):4806–4822. https://doi.org/10.1002/smll.201500802

Chatterjee S, Hui PC, Siu WS, Kan CW, Leung PC, Wanxue C, Chiou JC (2021) Influence of pH-responsive compounds synthesized from chitosan and hyaluronic acid on dual-responsive (pH/temperature) hydrogel drug delivery systems of Cortex Moutan. Int J Biol Macromol 168:163–174. https://doi.org/10.1016/j.ijbiomac.2020.12.035

Chen Y, Shi J (2016) Chemistry of mesoporous organosilica in nanotechnology: molecularly organic-inorganic hybridization into frameworks. Adv Mater 28(17):3235–3272. https://doi.org/10.1002/adma.201505147

Cheng Z, Al Zaki A, Hui JZ, Muzykantov VR, Tsourkas A (2012) Multifunctional nanoparticles: cost versus benefit of adding targeting and imaging capabilities. Science 338(6109):903–910. https://doi.org/10.1126/science.1226338

Croissant JG, Fatieiev Y, Almalik A, Khashab NM (2018) Mesoporous silica and organosilica nanoparticles: physical chemistry, biosafety, delivery strategies, and biomedical applications. Adv Healthc Mater. https://doi.org/10.1002/adhm.201700831

Golombek SK, May JN, Theek B, Appold L, Drude N, Kiessling F, Lammers T (2018) Tumor targeting via EPR: strategies to enhance patient responses. Adv Drug Deliv Rev 130:17–38. https://doi.org/10.1016/j.addr.2018.07.007

He Y, Nie Y, Cheng G, Xie L, Shen Y, Gu Z (2014) Viral mimicking ternary polyplexes: a reduction-controlled hierarchical unpacking vector for gene delivery. Adv Mater 26(10):1534–1540. https://doi.org/10.1002/adma.201304592

Huang P, Chen Y, Lin H, Yu L, Zhang L, Wang L, Zhu Y, Shi J (2017) Molecularly organic/inorganic hybrid hollow mesoporous organosilica nanocapsules with tumor-specific biodegradability and enhanced chemotherapeutic functionality. Biomaterials 125:23–37. https://doi.org/10.1016/j.biomaterials.2017.02.018

Ji Y, Liu X, Huang M, Jiang J, Liao YP, Liu Q, Chang CH, Liao H, Lu J, Wang X, Spencer MJ, Meng H (2019) Development of self-assembled multi-arm polyrotaxanes nanocarriers for systemic plasmid delivery in vivo. Biomaterials 192:416–428. https://doi.org/10.1016/j.biomaterials.2018.11.027

Jin Y, Yang X, Tian J (2018) Targeted polypyrrole nanoparticles for the identification and treatment of hepatocellular carcinoma. Nanoscale 10(20):9594–9601. https://doi.org/10.1039/c8nr02036a

Kamel NM, Helmy MW, Abdelfattah EZ, Khattab SN, Ragab D, Samaha MW, Fang JY, Elzoghby AO (2020) Inhalable dual-targeted hybrid lipid nanocore-protein shell composites for combined delivery of genistein and all-trans retinoic acid to lung cancer cells. ACS Biomater Sci Eng 6(1):71–87. https://doi.org/10.1021/acsbiomaterials.8b01374

Kim D, Shin K, Kwon SG, Hyeon T (2018) Synthesis and biomedical applications of multifunctional nanoparticles. Adv Mater 30(49):e1802309. https://doi.org/10.1002/adma.201802309

Kong FH, Ye QF, Miao XY, Liu X, Huang SQ, Xiong L, Wen Y, Zhang ZJ (2021) Current status of sorafenib nanoparticle delivery systems in the treatment of hepatocellular carcinoma. Theranostics 11(11):5464–5490. https://doi.org/10.7150/thno.54822

Kulik L, El-Serag HB (2019) Epidemiology and management of hepatocellular carcinoma. Gastroenterology 156(2):477-491 e471. https://doi.org/10.1053/j.gastro.2018.08.065

Laksee S, Sansanaphongpricha K, Puthong S, Sangphech N, Palaga T, Muangsin N (2020) New organic/inorganic nanohybrids of targeted pullulan derivative/gold nanoparticles for effective drug delivery systems. Int J Biol Macromol 162:561–577. https://doi.org/10.1016/j.ijbiomac.2020.06.089

Lei W, Sun C, Jiang T, Gao Y, Yang Y, Zhao Q, Wang S (2019) Polydopamine-coated mesoporous silica nanoparticles for multi-responsive drug delivery and combined chemo-photothermal therapy. Mater Sci Eng C Mater Biol Appl 105:110103. https://doi.org/10.1016/j.msec.2019.110103

Li J, Wang X, Zhao G, Chen C, Chai Z, Alsaedi A, Hayat T, Wang X (2018) Metal-organic framework-based materials: superior adsorbents for the capture of toxic and radioactive metal ions. Chem Soc Rev 47(7):2322–2356. https://doi.org/10.1039/c7cs00543a

Li J, Meng Z, Brett DJL, Shearing PR, Skipper NT, Parkin IP, Gadipelli S (2020) High-performance zinc-air batteries with scalable metal-organic frameworks and platinum carbon black bifunctional catalysts. ACS Appl Mater Interfaces 12(38):42696–42703. https://doi.org/10.1021/acsami.0c10151

Lo A, Lin CT, Wu HC (2008) Hepatocellular carcinoma cell-specific peptide ligand for targeted drug delivery. Mol Cancer Ther 7(3):579–589. https://doi.org/10.1158/1535-7163.MCT-07-2359

Lv L, Shi Y, Wu J, Li G (2021) Nanosized drug delivery systems for breast cancer stem cell targeting. Int J Nanomed 16:1487–1508. https://doi.org/10.2147/IJN.S282110

Lyu N, Kong Y, Mu L, Lin Y, Li J, Liu Y, Zhang Z, Zheng L, Deng H, Li S, Xie Q, Guo R, Shi M, Xu L, Cai X, Wu P, Zhao M (2018) Hepatic arterial infusion of oxaliplatin plus fluorouracil/leucovorin vs sorafenib for advanced hepatocellular carcinoma. J Hepatol 69(1):60–69. https://doi.org/10.1016/j.jhep.2018.02.008

Maity A, Belgamwar R, Polshettiwar V (2019) Facile synthesis to tune size, textural properties and fiber density of dendritic fibrous nanosilica for applications in catalysis and CO2 capture. Nat Protoc 14(7):2177–2204. https://doi.org/10.1038/s41596-019-0177-z

Mirzaghavami PS, Khoei S, Khoee S, Shirvalilou S (2022) Folic acid-conjugated magnetic triblock copolymer nanoparticles for dual targeted delivery of 5-fluorouracil to colon cancer cells. Cancer Nanotechnol. https://doi.org/10.1186/s12645-022-00120-3

Mo ZC, Ren K, Liu X, Tang ZL, Yi GH (2016) A high-density lipoprotein-mediated drug delivery system. Adv Drug Deliv Rev 106(Pt A):132–147. https://doi.org/10.1016/j.addr.2016.04.030

Plemel JR, Caprariello AV, Keough MB, Henry TJ, Tsutsui S, Chu TH, Schenk GJ, Klaver R, Yong VW, Stys PK (2017) Unique spectral signatures of the nucleic acid dye acridine orange can distinguish cell death by apoptosis and necroptosis. J Cell Biol 216(4):1163–1181. https://doi.org/10.1083/jcb.201602028

Ponton I, Marti Del Rio A, Gomez Gomez M, Sanchez-Garcia D (2020) Preparation and applications of organo-silica hybrid mesoporous silica nanoparticles for the co-delivery of drugs and nucleic acids. Nanomaterials. https://doi.org/10.3390/nano10122466

Samji H, Yu A, Kuo M, Alavi M, Woods R, Alvarez M, Dore GJ, Tyndall M, Krajden M, Janjua NZ, Team BCHTC (2017) Late hepatitis B and C diagnosis in relation to disease decompensation and hepatocellular carcinoma development. J Hepatol 67(5):909–917. https://doi.org/10.1016/j.jhep.2017.06.025

Sardoiwala MN, Kushwaha AC, Dev A, Shrimali N, Guchhait P, Karmakar S, Roy Choudhury S (2020) Hypericin-loaded transferrin nanoparticles induce PP2A-regulated BMI1 degradation in colorectal cancer-specific chemo-photodynamic therapy. ACS Biomater Sci Eng 6(5):3139–3153. https://doi.org/10.1021/acsbiomaterials.9b01844

Sayiner M, Golabi P, Younossi ZM (2019) Disease burden of hepatocellular carcinoma: a global perspective. Dig Dis Sci 64(4):910–917. https://doi.org/10.1007/s10620-019-05537-2

Shen Z, Chen T, Ma X, Ren W, Zhou Z, Zhu G, Zhang A, Liu Y, Song J, Li Z, Ruan H, Fan W, Lin L, Munasinghe J, Chen X, Wu A (2017) Multifunctional theranostic nanoparticles based on exceedingly small magnetic iron oxide nanoparticles for T1-weighted magnetic resonance imaging and chemotherapy. ACS Nano 11(11):10992–11004. https://doi.org/10.1021/acsnano.7b04924

Simon TG, Duberg AS, Aleman S, Chung RT, Chan AT, Ludvigsson JF (2020) Association of aspirin with hepatocellular carcinoma and liver-related mortality. N Engl J Med 382(11):1018–1028. https://doi.org/10.1056/NEJMoa1912035

Singh N, Sahoo SK, Kumar R (2020) Hemolysis tendency of anticancer nanoparticles changes with type of blood group antigen: an insight into blood nanoparticle interactions. Mater Sci Eng C Mater Biol Appl 109:110645. https://doi.org/10.1016/j.msec.2020.110645

Teng Z, Li W, Tang Y, Elzatahry A, Lu G, Zhao D (2019) Mesoporous Organosilica hollow nanoparticles: synthesis and applications. Adv Mater 31(38):e1707612. https://doi.org/10.1002/adma.201707612

Wang D, Liu B, Ma Y, Wu C, Mou Q, Deng H, Wang R, Yan D, Zhang C, Zhu X (2017) A molecular recognition approach to synthesize nucleoside analogue based multifunctional nanoparticles for targeted cancer therapy. J Am Chem Soc 139(40):14021–14024. https://doi.org/10.1021/jacs.7b08303

Wang C, Sudlow G, Wang Z, Cao S, Jiang Q, Neiner A, Morrissey JJ, Kharasch ED, Achilefu S, Singamaneni S (2018) Metal-organic framework encapsulation preserves the bioactivity of protein therapeutics. Adv Healthc Mater 7(22):e1800950. https://doi.org/10.1002/adhm.201800950

Wang Y, Wu W, Liu J, Manghnani PN, Hu F, Ma D, Teh C, Wang B, Liu B (2019) Cancer-cell-activated photodynamic therapy assisted by Cu(II)-based metal-organic framework. ACS Nano 13(6):6879–6890. https://doi.org/10.1021/acsnano.9b01665

Xie M, Li J, Deng T, Yang N, Yang M (2021) Modification of magnetic molybdenum disulfide by chitosan/carboxymethylcellulose with enhanced dispersibility for targeted photothermal-/chemotherapy of cancer. J Mater Chem B 9(7):1833–1845. https://doi.org/10.1039/d0tb01664k

Xu Q, Yang Y, Lu J, Lin Y, Feng S, Luo X, Di D, Wang S, Zhao Q (2022) Recent trends of mesoporous silica-based nanoplatforms for nanodynamic therapies. Coord Chem Rev. https://doi.org/10.1016/j.ccr.2022.214687

Yang S, Li Y (2020) Fluorescent hybrid silica nanoparticles and their biomedical applications. Wiley Interdiscip Rev Nanomed Nanobiotechnol 12(3):e1603. https://doi.org/10.1002/wnan.1603

Yang S, Li D, Chen L, Zhou X, Fu L, You Y, You Z, Kang L, Li M, He C (2021) Coupling metal organic frameworks with molybdenum disulfide nanoflakes for targeted cancer theranostics. Biomater Sci 9(9):3306–3318. https://doi.org/10.1039/d0bm02012e

Yu L, Chen Y, Lin H, Du W, Chen H, Shi J (2018) Ultrasmall mesoporous organosilica nanoparticles: Morphology modulations and redox-responsive biodegradability for tumor-specific drug delivery. Biomaterials 161:292–305. https://doi.org/10.1016/j.biomaterials.2018.01.046

Zhang Q, Jiang Q, Li N, Dai L, Liu Q, Song L, Wang J, Li Y, Tian J, Ding B, Du Y (2014) DNA origami as an in vivo drug delivery vehicle for cancer therapy. ACS Nano 8(7):6633–6643. https://doi.org/10.1021/nn502058j

Zhang M, Cao Y, Wang L, Ma Y, Tu X, Zhang Z (2015) Manganese doped iron oxide theranostic nanoparticles for combined T1 magnetic resonance imaging and photothermal therapy. ACS Appl Mater Interfaces 7(8):4650–4658. https://doi.org/10.1021/am5080453

Zhang L, Jean SR, Ahmed S, Aldridge PM, Li X, Fan F, Sargent EH, Kelley SO (2017) Multifunctional quantum dot DNA hydrogels. Nat Commun 8(1):381. https://doi.org/10.1038/s41467-017-00298-w

Zhou J, Ding L, Zhu Y, Wang B, Li X, Zhang J (2020) Comparative thermal research on tetraazapentalene-derived heat-resistant energetic structures. Sci Rep 10(1):21757. https://doi.org/10.1038/s41598-020-78980-1

Publisher's Note